Dynamics of Deep Recirculation Cells Offshore of the Deep Western Boundary Current in the Subtropical North Atlantic (15°–30°N)

TIAGO CARRILHO BILÓ,[a,b] WILLIAM E JOHNS,[b] AND JIAN ZHAO[c]

[a] *Scripps Institution of Oceanography, University California, San Diego, La Jolla, California*
[b] *Rosenstiel School of Marine and Atmospheric Science, University of Miami, Miami, Florida*
[c] *Horn Point Laboratory, University of Maryland Center for Environmental Science, Cambridge, Maryland*

ABSTRACT: The dynamics of the deep recirculation offshore of the deep western boundary current (DWBC) between 15° and 30°N within the upper North Atlantic Deep Water layer ($1000 \leq z \leq 3000$ m) is investigated with two different eddy-resolving numerical simulations. Despite some differences in the recirculation cells, our assessment of the modeled deep isopycnal circulation patterns ($36.77 \leq \sigma_2 \leq 37.06$ kg m^{-3}) shows that both simulations predict the DWBC flowing southward along the continental slope, while the so-called Abaco Gyre and two additional cyclonic cells recirculate waters northward in the interior. These cells are a few degrees wide, located along the DWBC path, and characterized by potential vorticity (PV) changes occurring along their mean streamlines. The analysis of the mean PV budget reveals that these changes result from the action of eddy forcing that tends to erode the PV horizontal gradients. The lack of a major upper-ocean boundary current within the study region, and the fact that the strongest eddy forcing is constrained within a few hundreds of kilometers of the western boundary, suggest that the DWBC is the primary source of eddy forcing. Finally, the eddies responsible for forcing the recirculation have dominant time scales between 100 and 300 days, which correspond to the primary observed variability scales of the DWBC transport at 26.5°N.

KEYWORDS: Abyssal circulation; Dynamics; Mesoscale processes; Ocean circulation; Ocean dynamics; Potential vorticity

1. Introduction

In the Atlantic Ocean, the North Atlantic Deep Water (NADW) formed at high latitudes spreads southward within the lower limb ($z > 1000$ m) of the Atlantic meridional overturning circulation (e.g., Talley et al. 2011). The NADW circulation consists of the deep western boundary current (DWBC) flowing southward along the Americas' continental slope, interior pathways, and multiple recirculation gyres (e.g., Schmitz and McCartney 1993; Lozier 1997; Garzoli et al. 2015; Biló and Johns 2019). The latter promote connectivity between the ocean's western boundary and interior, and significantly modify the DWBC's transport at certain locations (e.g., Johns et al. 2008; Toole et al. 2017). Observations and numerical experiments show that, between 15° and 30°N, the interior NADW circulation is characterized by multiple localized (i.e., few degrees wide) cyclonic recirculation cells along the western boundary embedded in a larger-scale recirculation (e.g., Fig. 1). Although the dynamical mechanisms that force deep ocean recirculation has been an active research area since the late 1970s [see compilation in Hogg and Johns (1995)], efforts to understand these particular cyclonic features are lacking thus far. Therefore, in this study, we use numerical eddy-resolving simulations to investigate the dynamics and forcing mechanisms responsible

for the northward recirculation adjacent to the western boundary at 15°–30°N.

Several studies have reported that the dynamics of deep recirculation gyres—and their interactions with the DWBC—are usually associated with the upper-ocean eddy activity. Offshore of the Grand Banks (~42°–50°N), part of the DWBC gets entrained in the deep portion of the northward North Atlantic Current and recirculates anticyclonically in the interior (Lozier 1997). Using numerical eddy-permitting and eddy-resolving global simulations, Gary et al. (2011) showed that this deep anticyclonic gyre seems to be eddy driven. Since this circulation feature is located in the vicinity of the highly variable surface intensified North Atlantic Current, the authors reasonably speculated its associated mesoscale activity forces the deep recirculation. Farther south and west (~35°–42°N, ~50°–75°W), the unstable Gulf Stream forces a nearly barotropic cyclonic gyre referred as to the Northern Recirculation Gyre (e.g., Hogg 1983; Hogg et al. 1986). The idealized numerical experiments performed by Le Bras et al. (2018) revealed that the proximity of its northern limit to the western boundary not only affects the DWBC transport but that interactions with the DWBC and bottom topography result in significant changes in the gyre mean structure. Near Cape Hatteras (~35°N), the southward DWBC is forced to cross under the northeastward Gulf Stream. Cruise-based observations and numerical simulations suggest that Gulf Stream meandering helps to trigger the upper DWBC to entrain under the Gulf Stream, flow offshore, and recirculate back to the western boundary (Pickart and Smethie 1993; Spall 1996; Bower and Hunt 2000).

Between 15° and 30°N, the interior mean deep circulation is complex and consists of multiple localized cyclonic cells along
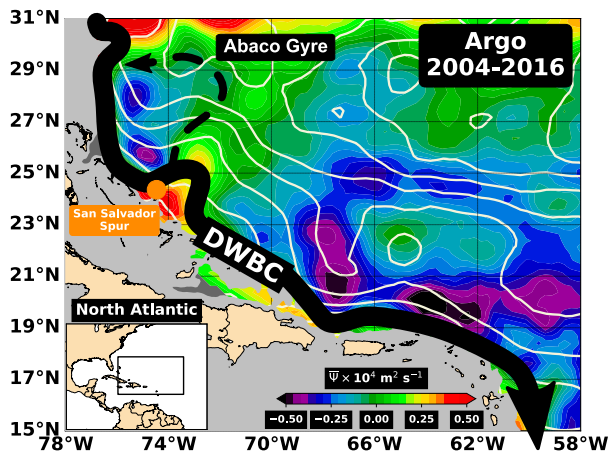
FIG. 1. Argo-based climatological mean (2004–16) absolute geostrophic streamfunction $\overline{\psi}$ (color scale) at the $\sigma_2 = 36.88$ kg m^{-3} isopycnal level in the western North Atlantic between 15° and 30°N derived by Biló and Johns (2019). The authors defined $\overline{\psi}$ such that local minima represent cyclonic circulation. The white lines represent the Argo-based climatological mean Ertel's PV lines equally spaced in 1×10^{-12} m^{-1} s^{-1}. PV generally increases northwestward in the domain with minimum values occurring near the western boundary. The thick black arrow indicates the DWBC flow that is not fully resolved by the Argo array. The thin dashed arrow highlights the Abaco Gyre recirculation. The Caribbean Sea and depths less than 3000 m are masked in light gray (topography taken from the General Bathymetric Chart of the Oceans; http://gebco.net).

the western boundary embedded in a basinwide recirculation (e.g., Xu et al. 2012; Biló and Johns 2019). The Argo-based deep circulation obtained by Biló and Johns (2019) shows that the potential vorticity (PV) is not conserved along mean geostrophic streamlines within these cells (Fig. 1), therefore an active forcing mechanism is required for maintaining them (Rhines and Holland 1979; Holland and Rhines 1980). Thus far, the most studied gyre in Fig. 1 is the northern cell, referred as to Abaco Gyre (25°–30°N), mostly in the context of monitoring the DWBC and adjacent meridional circulation at 26.5°N (e.g., Lee et al. 1990, 1996; Bryden et al. 2005; Johns et al. 2008; Meinen et al. 2013). Analyzing nearly two decades of velocity and hydrographic observations, Biló and Johns (2020) concluded that 20%–50% of the mean DWBC's transport (~30 Sv; 1 Sv ≡ 10^6 m^3 s^{-1}) is recirculating northward at 26.5°N in the Abaco Gyre.

Based on highly variable 1.5-yr-long current records, Lee et al. (1990) were the first to speculate that the Abaco Gyre could be eddy driven. However, Leaman and Vertes (1996) was the first and only study to directly address the possible dynamics behind the recirculation in the region. Analyzing deep Lagrangian floats trajectories released in the DWBC domain, the authors found that the trajectories were dominated by eddy motions, which helped to export the floats to the interior. Their analysis also suggested that the San Salvador Spur (see Fig. 1) plays a major role in forcing the flow to recirculate cyclonically.

In the present study, we test the hypothesis that mesoscale eddies drive the deep localized cyclonic cells along the DWBC path between 15° and 30°N. Using two different numerical

models, we assess the DWBC recirculation forcing in terms of PV dynamics (Rhines and Holland 1979; Holland and Rhines 1980; Hogg 1983; Hogg and Johns 1995; Pickart and Smethie 1993; Spall 1996), and show that local eddy PV fluxes are mainly responsible for driving these deep recirculation gyres. We also show that the perturbations responsible for modifying the PV of the mean flow likely originate within the western boundary layer.

2. Models and methods

To reduce the likelihood that our analysis and dynamical interpretations are model dependent, we use two eddy-resolving simulations that are similarly forced (i.e., wind forcing and surfaces fluxes), but that use different architectures (i.e., z-grid and hybrid vertical coordinates), initialization procedures, integration periods, spatial coverage, and horizontal resolution.

a. Model 1: HYCOM

The first numerical simulation used in this study was performed by Zhao et al. (2018a). The authors used the Hybrid Coordinate Ocean Model (HYCOM) with a horizontal resolution of 1/12°, 32 vertical layers—i.e., isopycnal layers far from model boundaries—in a domain spanning 28°S–80°N. The model was configured following Xu et al. (2010) and initialized using the 25-yr spun-up climatological experiment E026 from Xu et al. (2012). The simulation was then spun up for an additional 25 years by repeatedly using the daily 1992 atmospheric forcing from the National Centers for Environmental Prediction (NCEP) Reanalysis data. After the spinup procedure, the model was integrated between 1992 and 2016, forced by the NCEP Reanalysis daily data. We chose this particular HYCOM simulation because its configuration successfully reproduced several important features of the large-scale circulation and mesoscale variability in the North Atlantic ocean (e.g., Xu et al. 2010, 2012, 2013; Zhao et al. 2018a,b). Model outputs consist of snapshots every 10 days from January 2000 to December 2016. HYCOM's source code is freely available at https://www.hycom.org/hycom/source-code.

b. Model 2: OFES

The second set of numerical outputs is from the eddy-resolving Ocean Model for the Earth Simulator (OFES) run by the Japan Agency for Marine-Earth Science and Technology. OFES is a z-grid coordinate model based on the Modular Ocean Model version 3, with 54 vertical levels, a horizontal resolution of 0.1°, and global coverage (Masumoto et al. 2004; Sasai et al. 2004; Sasaki et al. 2008). This simulation was initialized using the *World Ocean Atlas 1998* climatology and forced by the NCEP Reanalysis data. OFES snapshots are available every 3 days from January 1980 to December 2013. Similar to HYCOM, these OFES predictions have been successfully used in Atlantic circulation studies (e.g., van Sebille et al. 2011, 2012; Meinen and Garzoli 2014). More recently, Biló and Johns (2020) found that the long-term mean and variability of the DWBC transport and deep velocities ($z > 1000$ m) predicted by OFES are in good agreement
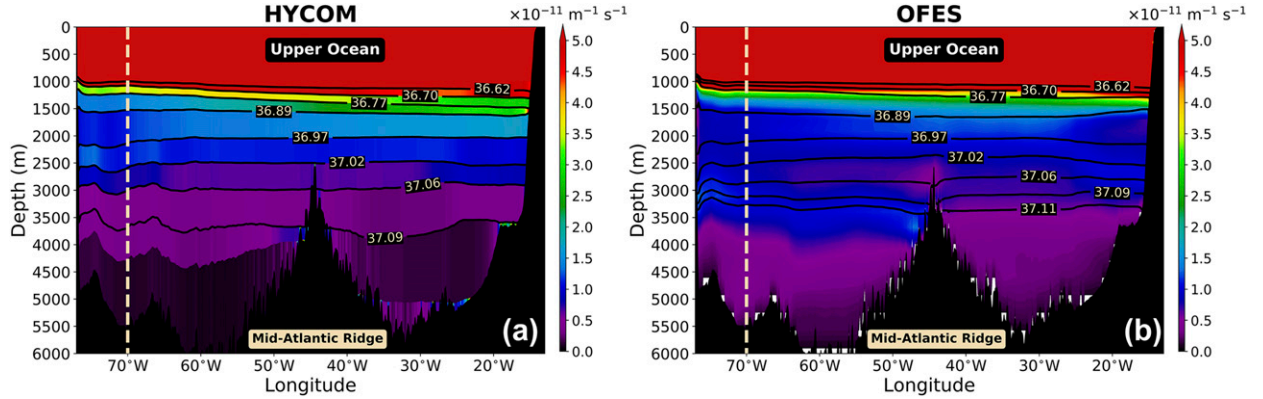
FIG. 2. Mean potential vorticity at 26.5°N in (a) HYCOM (2000–16) and (b) OFES (1980–2013). The color scale was chosen to highlight the PV gradients in the deep ocean ($z > 1000$ m). The solid horizontal lines are the σ_2 isopycnals. The σ_2 values 36.62, 36.70, 36.77, 36.89, 36.97, 37.02, 37.06, 37.09, and 37.11 kg m^{-3} represent some of the HYCOM's density interfaces. The dashed vertical lines indicate the 70°W longitude.

with observations at 26.5°N. For further details on OFES and data access see http://www.jamstec.go.jp/esc/research/AtmOcn/product/ofes.html.

c. The mean potential vorticity PV budget

PV (q) is a dynamical tracer that is conserved in the absence of forcing or dissipation. Therefore, in large-scale and mesoscale ocean dynamics, the PV conservation equation is

$$\frac{\partial q}{\partial t} + \mathbf{u} \cdot \nabla q = S, \tag{1}$$

where $\mathbf{u}$ is the horizontal velocity vector, ∇ is the horizontal gradient operator, and S represents sources/sinks of PV. Decomposing the variables into time-mean and perturbation (i.e., deviation from the mean) components, and averaging the resulting expression over time we obtain

$$\overline{\mathbf{u}} \cdot \nabla \overline{q} = -\nabla \cdot (\overline{\mathbf{u}'q'}) + \overline{S}, \tag{2}$$

where time averages are indicated by overbars, and perturbations (or eddy terms) by the primes. The left-hand side is the mean PV advection, the first term on the right-hand side is the convergence of eddy PV fluxes $\overline{\mathbf{u}'q'}$, and the last term is the mean sources/sinks due to mainly frictional and diabatic processes (e.g., Rhines and Holland 1979). This simple equation is the theoretical cornerstone of eddy-driven circulation, and its dynamical consequences were explored by Rhines and Holland (1979). The authors show that mean circulation can be forced to cross PV isolines by the convergence or divergence of eddy fluxes, implying a balance between the first two terms of Eq. (2). This dynamical balance is referred as to the turbulent Sverdrup balance.

In this study, we define PV as the Ertel's PV for large-scale and mesoscale flows (e.g., Pedlosky 1987):

$$q = -\frac{(f + \zeta)}{\rho}\frac{\partial \sigma}{\partial z}, \tag{3}$$

where f is the Coriolis parameter, $\zeta = (\partial v/\partial x) - (\partial u/\partial y)$ is the vertical component of the relative vorticity, ρ is density, σ is the

potential density, and z is the vertical coordinate. Based on Eq. (3) and defining the thickness term of PV $T_h = (1/\rho)(\partial \sigma/\partial z)$, q' can be explicitly written as

$$q' = -\zeta'(T_h' + \overline{T_h}) - (f + \overline{\zeta})T_h'. \tag{4}$$

Therefore, the $\overline{\mathbf{u}'q'}$ in Eq. (2) becomes

$$\overline{\mathbf{u}'q'} = -\overline{\mathbf{u}'\zeta'T_h'} - (f + \overline{\zeta})\overline{\mathbf{u}'T_h'} - \overline{T_h}\,\overline{\mathbf{u}'\zeta'}, \tag{5}$$

where the second and third terms in the right-hand side of Eq. (5) are known as eddy thickness and eddy relative vorticity fluxes, respectively. The first term, a triple correlation, is usually assumed to be negligible when compared to the other double primed terms and can formally be assumed so for small-amplitude fluctuations.

Similar to several studies that investigated the dynamics of deep recirculation in other regions (e.g., Holland and Rhines 1980; Spall 1994, 1996; Qiu et al. 2008; van Sebille et al. 2012), we validate the turbulent Sverdrup balance [Eq. (2)] and diagnose the eddy PV fluxes from numerical simulations within the localized DWBC recirculation cells.

d. The layer approach

To learn how different HYCOM and OFES are in terms of vertical structure, Fig. 2 shows the mean PV distribution and stratification along 26.5°N from both numerical models. Although the water masses below 3000-m depth are noticeably lighter in HYCOM (see areas $\sigma_2 > 37.06$ kg m^{-3}), the stratification—and consequently PV—is generally consistent between 1000- and 3000-m depth. Note that Eq. (3) defines Ertel's PV for a continually stratified ocean. Therefore, we modified Eq. (3) so that HYCOM's PV could be expressed in terms of an equivalent Ertel PV by $-[(f + \zeta_i)/\rho_i](\Delta\sigma_i/h_i)$, where i is the layer index, $\Delta\sigma_i = \sigma_{i+1} - \sigma_i$ is the density jump within the layer, and h is the layer thickness.

To keep our analysis consistent, we averaged the OFES outputs over the isopycnal layers defined in HYCOM. We focus our investigation on the layers constrained between

1000 and 3000 m in the study region (i.e., $36.77 \leq \sigma_2 \leq 37.06 \, \mathrm{kg \, m^{-3}}$). Vertical layers between 1000- and 3000-m depth mainly correspond to the upper NADW layer, which contains at least 60% of the total transport near the western boundary (e.g., Johns et al. 2008; Biló and Johns 2020). Throughout this paper, we describe the mean circulation within each layer in terms of streamfunction ψ. We estimated ψ (i.e., $v = \partial \psi / \partial x$ and $u = -\partial \psi / \partial y$) by decomposing the velocity vectors into their nondivergent and nonrotational components following Li et al. (2006). The same methodology was used to decompose the eddy PV fluxes $\overline{\mathbf{u}'q'}$. More details of this methodology can also be found in Biló and Johns (2019).

3. Results and discussion

a. The mean DWBC recirculation

Before proceeding with the PV analysis, it is necessary to establish if the numerical simulations reproduce key aspects of the observed long-term mean circulation in the study region. Figure 3 shows the simulated time-averaged streamfunction and PV within each layer. As suggested by Biló and Johns's (2019) observational analysis (e.g., Fig. 1), both models predict three main cyclonic recirculation areas along the western boundary and offshore of the DWBC. The northern cell, known as the Abaco Gyre, is constrained mainly between 25° and 30°N, with an indication in HYCOM of two semi-enclosed circulation centers near 26° and 28°N. Farther south (19°–24°N) along the western boundary, two additional cyclonic circulation cells are identified just offshore of the DWBC. A common characteristic in these cells is that the PV is not conserved along the recirculation gyres streamlines (i.e., $\overline{\mathbf{u}} \cdot \nabla \overline{q} \neq 0$). Since the Abaco Gyre circulation has been extensively observed at 26.5°N, additional comparison between the simulations and observations at 26.5°N can be found in the online supplemental material.

Both models show that the velocity structure and streamfunction patterns are vertically coherent over the upper NADW layer, but the lateral PV gradients significantly change their orientation with depth. Near the base of the thermocline the PV lines are mostly oriented southwest–northeast (Figs. 3a,b), while at $36.89 \leq \sigma_2 \leq 37.02 \, \mathrm{kg \, m^{-3}}$ the orientation is southeast–northwest (Figs. 3c–f). Below $\sigma_2 = 37.02 \, \mathrm{kg \, m^{-3}}$, the PV lines become oriented southwest–northeast again (Figs. 3g,h). Note that in the vicinity of the closed cyclonic circulation cells, PV gradients tend to be weaker, especially in HYCOM (Fig. 3, left panels). In the theoretical discussions carried out by Rhines and Young (1982), the authors show that, because eddies tend to flux PV downgradient, PV is often homogenized within closed circulation contours in the steady state.

These two particular numerical simulations do not perfectly agree, and noticeable differences in the circulation are present. For example, HYCOM's higher PV content (Fig. 2) and significantly larger horizontal PV gradient between $36.77 \leq \sigma_2 \leq 36.89 \, \mathrm{kg \, m^{-3}}$ (Figs. 3a,b) indicate the pycnocline is deeper than the one in OFES. In addition, the interior anticyclonic circulation between 23° and 29°N and 58° and

72°W (e.g., $\psi > 0.2 \times 10^4 \, \mathrm{m^2 \, s^{-1}}$ in Figs. 3a,c,e,g) is only apparent in OFES below $\sigma_2 = 37.02 \, \mathrm{kg \, m^{-3}}$ (Fig. 3h).

The details of the velocity structure of the recirculation along the western boundary are also different. For example, like the Argo-based circulation (Fig. 1), HYCOM shows an Abaco Gyre with two closed cyclonic cells while OFES presents only a single cell. The recirculation gyre between 21° and 24°N consists of a single cell in HYCOM but two partially connected cells in OFES. These differences will be reflected in the mean PV budget analysis described later in the paper. One can argue that the reason for this "disagreement" among models is due to the periods in which the outputs were averaged (i.e., HYCOM 2000–16 and OFES 1980–2013). Although OFES's long-term average includes more than 30 years, 17-yr averages of its outputs (not shown) do not significantly change the overall circulation patterns presented in Fig. 3 (right panels). Such differences are probably related to the setup of each model and their respective initialization procedures. Further, Xu et al. (2010) originally designed this HYCOM configuration to study the subpolar North Atlantic, whereas OFES is a global simulation. Despite these differences, both models show recirculation features that qualitatively resemble those found in the observations, and so are suitable for investigating the underlying dynamics of these features.

b. The turbulent Sverdrup balance

Using the PV definition from Eq. (3) in Eq. (2), it is possible to evaluate how much of the mean PV advection can be explained by the eddy forcing term. To take into account the differences in the models, we focus the PV budget analysis on the layer containing the DWBC velocity core and strongest recirculation signal in each model (i.e., $36.97 \leq \sigma_2 \leq 37.02 \, \mathrm{kg \, m^{-3}}$ in HYCOM, and $36.89 \leq \sigma_2 \leq 36.97 \, \mathrm{kg \, m^{-3}}$ in OFES).

Figures 4 and 5 show that the eddy flux convergence qualitatively explains the spatial distribution of mean PV advection in both models (see panels a and b). Although the details differ, there is a clear tendency for the eddy PV fluxes to force the mean flow to lose PV along the path of the DWBC ($\overline{\mathbf{u}} \cdot \nabla \overline{q} < 0$), while gaining PV where the recirculated waters leave the western boundary ($\overline{\mathbf{u}} \cdot \nabla \overline{q} > 0$; e.g., Figs. 4a and 5a). The qualitative balance between these two terms of Eq. (2) is valid for all layers between $36.77 \leq \sigma_2 \leq 37.06 \, \mathrm{kg \, m^{-3}}$ (~1000–3000 m). Additionally, the eddy fluxes and consequently the flux convergences are dominated by the eddy PV thickness term [see Eq. (5) and Figs. 4c and 5c]. These eddy thickness fluxes are associated with eddy advection of layer thickness anomalies and are often found to dominate the total eddy PV flux in geophysical flows (e.g., Rhines and Holland 1979; Holland and Rhines 1980).

When extending the analysis to layers deeper than 3000 m the PV budget terms become noisier with no clear spatial correlation, suggesting other mechanisms in the $\overline{S}$ term in Eq. (2) may become more important near the ocean bottom. Moreover, the weak velocities and stratification in the deep ocean—as well as the coarser OFES vertical resolution below 2500 m ($\Delta z \sim 300 \, \mathrm{m}$)—can be a source of uncertainty in the computation of spatial gradients.
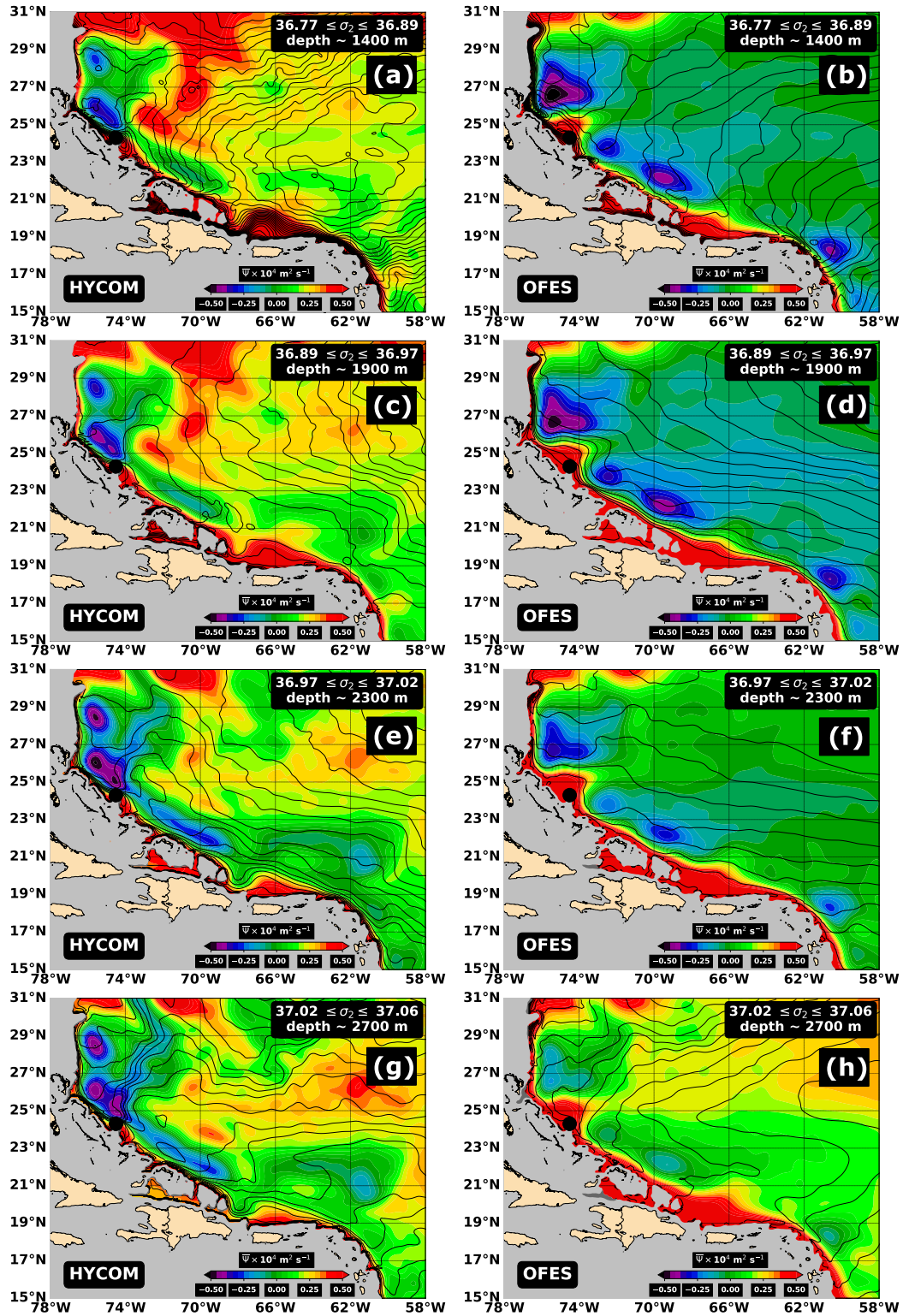
FIG. 3. Layer averaged streamfunction (color scale) from (a),(c),(e),(g) HYCOM 2000–16 and (b),(d),(f),(h) OFES 1980–2013. The black solid lines represent the mean PV lines equally spaced in $0.5 \times 10^{-12} \, \mathrm{m}^{-1} \, \mathrm{s}^{-1}$. PV mostly increases northward in the domain. The black dot indicates the location of the San Salvador Spur. Depths less than 3000 m are masked in light gray.
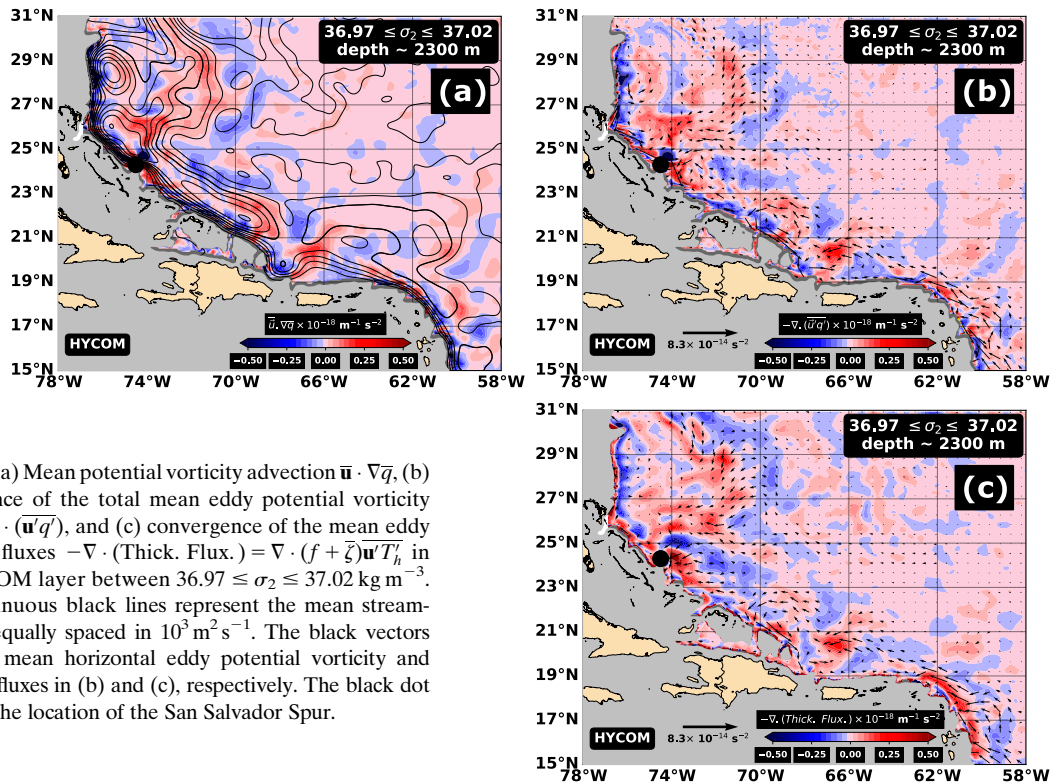
FIG. 4. (a) Mean potential vorticity advection $\overline{\mathbf{u}} \cdot \nabla \overline{q}$, (b) convergence of the total mean eddy potential vorticity fluxes $-\nabla \cdot (\overline{\mathbf{u}'q'})$, and (c) convergence of the mean eddy thickness fluxes $-\nabla \cdot (\text{Thick. Flux.}) = \nabla \cdot (f + \overline{\zeta})\overline{\mathbf{u}'T_h'}$ in the HYCOM layer between $36.97 \leq \sigma_2 \leq 37.02 \text{ kg m}^{-3}$. The continuous black lines represent the mean streamfunction equally spaced in $10^3 \text{ m}^2 \text{ s}^{-1}$. The black vectors show the mean horizontal eddy potential vorticity and thickness fluxes in (b) and (c), respectively. The black dot indicates the location of the San Salvador Spur.

The eddy fluxes and their respective convergence patterns are most intense near and along the western boundary (Figs. 4b,c and 5b,c), especially south of 25°N. The exception is the relatively large southward fluxes between 70° and 72°W and between 27° and 30°N in HYCOM. These eddy fluxes generate an enhanced positive convergence corridor, which is not obvious in OFES. Figure 3 shows that the HYCOM's PV gradient over this area is noticeably larger than in OFES, generating larger PV perturbations. This corridor, however, is present in deeper OFES layers $\sigma_2 > 37.02 \text{ kg m}^{-3}$ (not shown). The OFES mean circulation analysis of the Abaco Gyre performed by Biló and Johns (2020) indicated that the velocity becomes more topographically constrained at depths larger than 3000 m. The region 70°–72°W and 27°–30°N is immediately east of a meridionally oriented topographic ridge known as the Bahama Ridge (e.g., Johns et al. 1997). This large flux convergence corridor is meridionally aligned along with this prominent topographic feature, suggesting that the ridge is significantly impacting HYCOM's circulation even above 3000-m depth.

To quantitatively assess how well the turbulent Sverdrup balance holds within the area depicted in Figs. 3–5, we calculated the three-dimensional linear spatial correlation coefficient of the two mean PV budget terms. Taking into account the entire study area for the density layers comprising $36.77 \leq \sigma_2 \leq 37.02 \text{ kg m}^{-3}$, the correlation coefficient is approximately 0.23 and 0.65 for HYCOM (Fig. 6a) and OFES (Fig. 6d), respectively. A more detailed analysis in each layer reveals that the largest differences between the terms are confined near the

western boundary, similar to the findings of other studies that have assessed the mean PV budget from numerical simulations (e.g., Lozier and Riser 1989; Spall 1996). Therefore, repeating the correlation calculation excluding areas within 50 (Figs. 6b,e) and 150 km (Figs. 6c,f) from the western boundary, the correlation between the terms increases substantially. Much larger correlation values for HYCOM (0.81) and OFES (0.93) are found when considering areas at least 150 km from the boundary, indicating that the eddy forcing is the primary dynamical mechanism responsible for forcing mean flow across PV contours in the DWBC recirculation regions. It is worth mentioning that 150 km is the approximate average width of the DWBC southward jet (Lee et al. 1996; Bryden et al. 2005; Johns et al. 2008). If layers below 3000 m are included, the correlation also decreases in both models.

The PV imbalance near the boundary can be explained mainly by diffusive and frictional forcing contained in $\overline{S}$ in Eq. (2). $\overline{S}$ is strongly dependent on the vertical and horizontal velocity shears, which are largest near topographic boundaries. In both models, $\overline{S}$ is mainly accounted by (i) vertical mixing represented by a K-profile parameterization boundary layer mixing scheme (Large et al. 1994); and (ii) horizontal mixing and dissipation parameterized by horizontal Laplacian and scale-selective damping biharmonic operators (e.g., Maltrud et al. 1998; Xu et al. 2010). Figure 7a shows that the residual of $\overline{\mathbf{u}} \cdot \nabla \overline{q}$ and $-\nabla \cdot (\overline{\mathbf{u}'q'})$—corresponding to an estimate of $\overline{S}$—is mostly negative near the western boundary, and it decreases (i.e., magnitude increases) toward the boundary. Similar results were found by Spall (1996) in a three-layer primitive
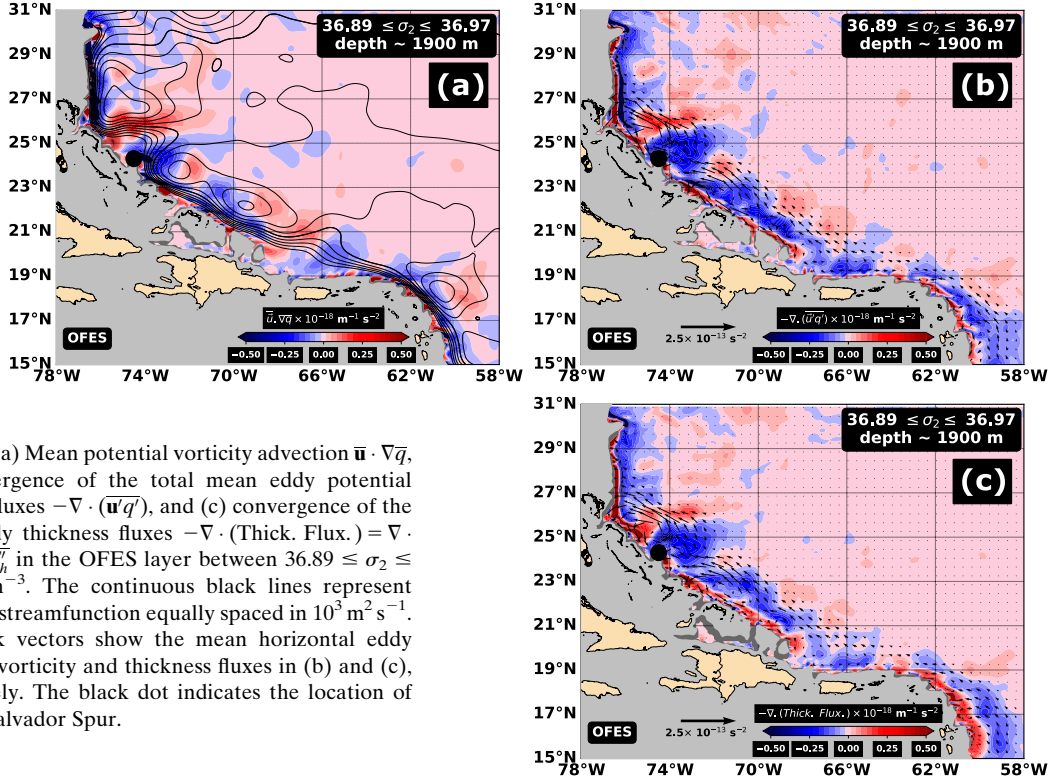
FIG. 5. (a) Mean potential vorticity advection $\overline{\mathbf{u}} \cdot \nabla \overline{q}$, (b) convergence of the total mean eddy potential vorticity fluxes $-\nabla \cdot (\overline{\mathbf{u}'q'})$, and (c) convergence of the mean eddy thickness fluxes $-\nabla \cdot$ (Thick. Flux.) $= \nabla \cdot (f + \overline{\zeta})\overline{\mathbf{u}'T_h'}$ in the OFES layer between $36.89 \leq \sigma_2 \leq 36.97 \text{ kg m}^{-3}$. The continuous black lines represent the mean streamfunction equally spaced in $10^3 \text{ m}^2 \text{ s}^{-1}$. The black vectors show the mean horizontal eddy potential vorticity and thickness fluxes in (b) and (c), respectively. The black dot indicates the location of the San Salvador Spur.

equations numerical model used to investigate the PV dynamics of the DWBC near Cape Hatteras. The author showed that the DWBC was allowed to flow southward under Gulf Stream because of the lateral frictional forcing (i.e., Laplacian diffusive operator) that dominated the PV budget near the boundary. A negative $\overline{S}$ band next to the boundary indicates that the mean DWBC flow loses PV, allowing the flow to continue southward without recirculating into the interior. Due to the consistency of the $\overline{S}$ sign within models, we believe a similar argument is valid for HYCOM and OFES between 15° and 30°N.

Taking into account the magnitude of the residual relative to mean PV advection term (Fig. 7b), it becomes clearer why the linear correlations shown in Fig. 6 are low when we include regions near the western boundary. Within 150 km from the boundary, the residual can be several times the mean PV advection term. In HYCOM, the residual around 130 km away from the boundary is still of the order of magnitude of the mean PV advection term, explaining the abrupt change in the correlations in Figs. 6b and 6c. OFES presents a gradual offshore decrease of this relative imbalance.

c. The eddy-driven mean circulation

The evaluation of Eq. (2) indicates the turbulent Sverdrup balance is valid outside the regions of active dissipation and mixing near the western boundary. Therefore, the eddy-driven velocity perpendicular to PV lines ($\overline{u}_\perp$) can be derived by dividing the eddy PV flux convergence by the magnitude of the mean potential vorticity gradient:

$$\overline{u}_\perp = \frac{-\nabla \cdot (\overline{\mathbf{u}'q'})}{|\nabla \overline{q}|}. \quad (6)$$

Following Rhines and Holland (1979), we integrated Eq. (6) pseudo-westward along constant $\overline{q}$ contours to reconstruct the eddy-driven mean streamfunction (Fig. 8). Overall, the eddy-forced circulation patterns are very similar (i.e., three recirculation gyres offshore the DWBC) but slightly weaker than those shown in Fig. 3. Besides the differences in the circulation strength, the eddy-driven Abaco Gyre structure in OFES is particularly distinct (Fig. 8b). Although the dimensions of the original and eddy-driven mean Abaco Gyre are generally consistent, the eddy-driven gyre is separated into three inner cyclonic closed cells (i.e., a northern cell and two adjacent cells between ~26° and 27°N). Additionally, the center of each closed eddy-driven cell is not perfectly aligned with the total $\overline{\psi}$ distribution.

It is worth mentioning that PV is a tracer estimated offline (i.e., not directly solved during model integration) and $\overline{\mathbf{u}} \cdot \nabla \overline{q}$ and $-\nabla \cdot (\overline{\mathbf{u}'q'})$ do not exactly balance each other in both simulations. Therefore, uncertainties arising from our calculation procedures and small imbalances of the PV budget terms are probably being accumulated for hundreds to a few thousands of kilometers. Additionally, HYCOM's horizontal PV gradients near the western boundary are significantly smaller than in offshore regions, leading to a loss of horizontal resolution over the localized recirculation cells. This loss of resolution is not as large in OFES; however, it is present within the Abaco Gyre (e.g., Fig. 3d, 25°–30°N). Together with the
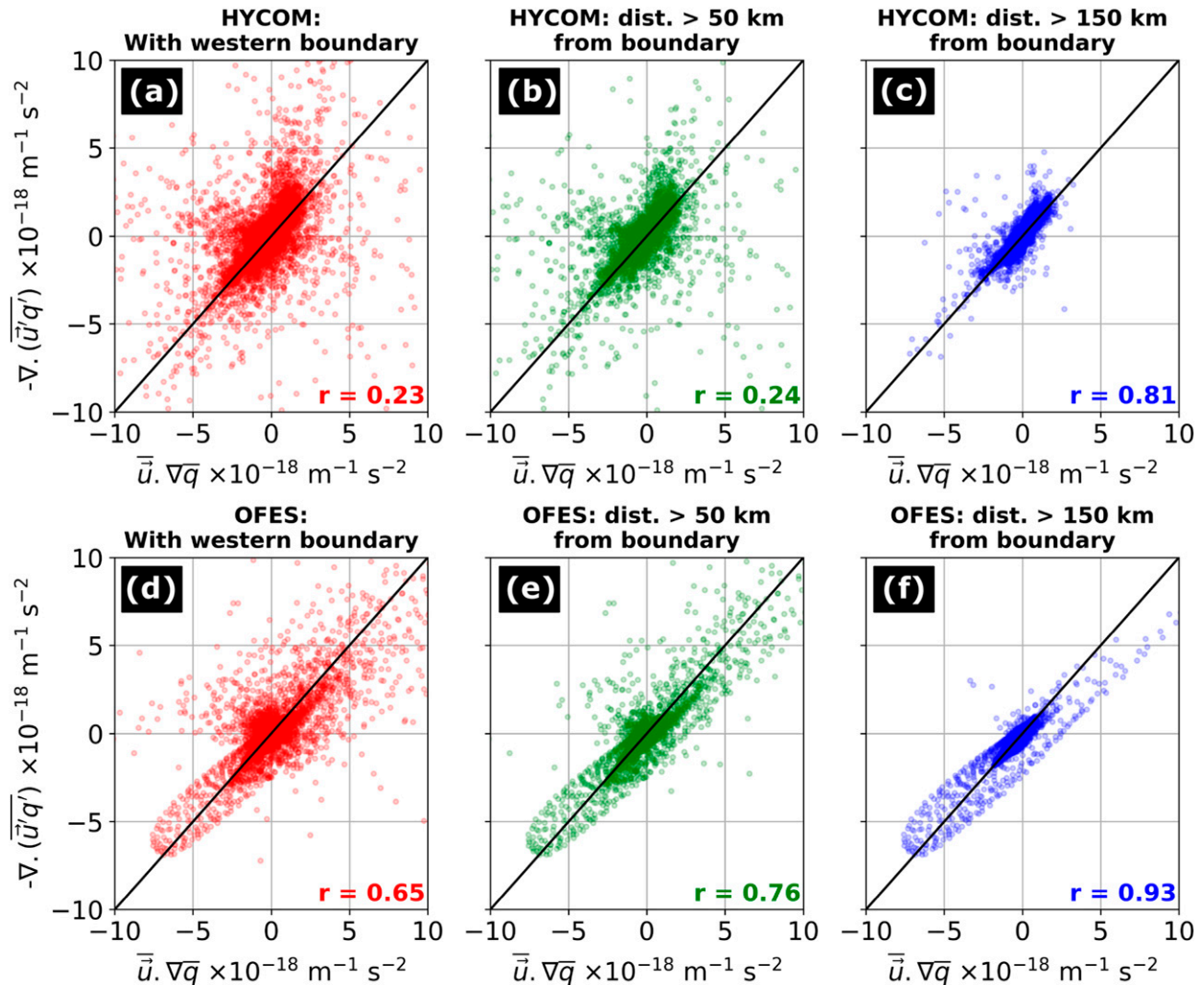
FIG. 6. Scatterplots of the mean potential vorticity advection $\overline{\mathbf{u}} \cdot \nabla \overline{q}$ vs the convergence of the mean eddy potential vorticity fluxes $-\nabla \cdot (\overline{\mathbf{u}'q'})$ at all grid points within 15°–31°N, 58°–77°W, and the four (a)–(c) HYCOM and (d)–(f) OFES layers between $36.77 \leq \sigma_2 \leq 37.06$ kg m^{-3}. The number in the lower-right corner of each panel represents the linear correlation between the two potential vorticity budget terms. The abbreviation dist. stands for distance from the boundary. The western boundary (i.e., distance = 0 km) is taken at the 1000-m isobath.

$\overline{u}_\perp$ patchy distributions (e.g., Fig. 5), it might explain the presence of three closed cells within the Abaco Gyre.

d. Evaluation of eddy fluxes in terms of the effective Austausch coefficient

A natural question to ask in such an analysis is whether the eddy PV fluxes are fluxing PV downgradient, and therefore acting to waken the PV spatial gradients. Hence, it is useful to consider the Austausch coefficient (Aq):

$$\text{Aq} = \frac{-\overline{\mathbf{u}'q'} \cdot \nabla \overline{q}}{|\nabla \overline{q}|^2}. \tag{7}$$

As discussed by Holland and Rhines (1980), Aq not only shows whether the eddies are fluxing PV downgradient (Aq > 0) but also indicates areas of eddy growth and sources of enstrophy to

the mean flow (i.e., $\overline{q}'^2$). Figures 9a and 9b depict a complex Aq distribution in both simulations. Although most of the domain presents positive Aq, an alternating positive and negative Aq pattern is found within the localized DWBC recirculation regions of $O(10^3$–$10^4)$ m^2 s^{-1}. In OFES, offshore and northward limbs of the recirculation cells are even dominated by upgradient eddy fluxes that could, in principle, lead to the sharpening of the PV horizontal gradients in these areas.

Marshall and Shutts (1981) explored the concept of Aq and concluded that Aq < 0 does not necessarily imply that eddies are decaying and sharpening the mean PV horizontal gradients. The authors argue that upgradient eddy fluxes can result from the rotational (i.e., nondivergent), and mostly dynamically inert, component of the eddy PV fluxes. To test if Aq distributions are being affected by the rotational component of the eddy fluxes, we estimated its divergent component using
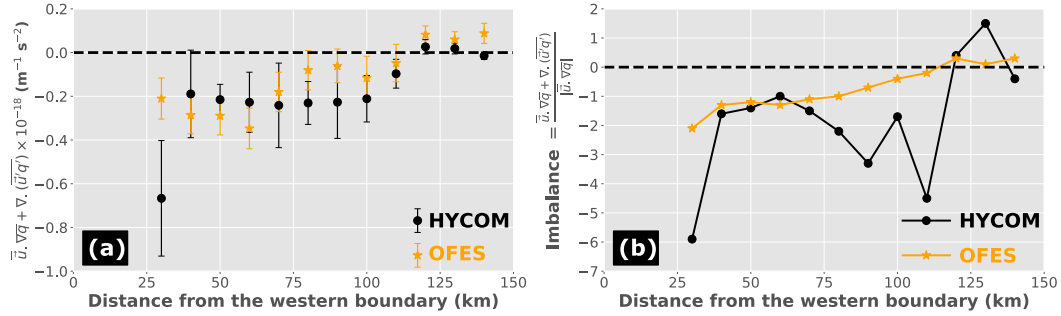
FIG. 7. (a) Residual of the main terms of the mean PV budget [i.e., $S \sim \overline{\mathbf{u}} \cdot \nabla \overline{q} + \nabla \cdot (\overline{\mathbf{u}'q'})$] and (b) the imbalance of these terms relative to the mean PV advection (i.e., residual/$|\overline{\mathbf{u}} \cdot \nabla \overline{q}|$) meridionally (15°–31°N) and vertically averaged ($36.77 \leq \sigma_2 \leq 37.06$ kg m^{-3}), as function of the distance from the western boundary. The western boundary (i.e., distance = 0 km) is taken at the 1000-m isobath. The error bars represent the standard error of the mean. Grid points less than 20 km from the western boundary were masked due to the change in the vertical coordinate system in HYCOM.

the Li et al. (2006) algorithm and recalculated Aq (Figs. 9c,d). The new coefficient (Aq)$_{\text{div}}$, based on only the divergent component of the eddy PV fluxes, is mainly positive over the entire domain; however, there are certain regions in OFES—offshore the San Salvador Spur ($\sim$24°N) and south of 19°N (Fig. 9d)—where it remains negative. Therefore, the dynamically active divergent component of the eddy PV fluxes (Fig. 10) is acting to homogenize the PV gradients within the recirculation gyres. Additionally, the perturbations responsible for these fluxes draw energy from and provide enstrophy to the mean flow along the western boundary and its vicinity (Holland and Rhines 1980).

e. Eddy sources and time scales

Analysis of the mean PV budget suggests that the DWBC localized cyclonic recirculation cells (Fig. 3) are being forced by the local convergence of eddy PV fluxes (Figs. 4 and 5). In contrast to other regions where deep recirculations are under the direct influence of major eddy-rich upper-ocean currents

(e.g., Gulf Stream and North Atlantic Current), the study area between 15° and 30°N is in a region of relatively weak upper-ocean currents. The most prominent upper-ocean circulation feature in the area is the Antilles Current, which flows northward in the upper 1000 m of the water column with maximum mean velocities and transports of approximately 0.3–0.5 m s^{-1} and 5 Sv, respectively (Meinen et al. 2019). Additionally, its velocity/transport fluctuations are significantly less intense than the Gulf Stream's—or North Atlantic Current's—fluctuations (e.g., Johns et al. 1995, 2008; Mertens et al. 2014).

Similar to the eddy-resolving simulation presented by Lüschow et al. (2019), the eddy kinetic energy (EKE $= \overline{u'^2 + v'^2}/2$) distributions in OFES and HYCOM (Fig. 11) corroborate the idea that the DWBC is the main source of eddy variability in the deep ocean within a few hundreds of kilometers from the western boundary south of 30°N. Figure 11 shows that the EKE within the recirculation gyres is $O(10^{-3}$–$10^{-2})$ m^2 s^{-2}, while farther offshore the EKE is $O(10^{-4}$–$10^{-3})$ m^2 s^{-2}. In both models, the higher levels of EKE near the San Salvador Spur is

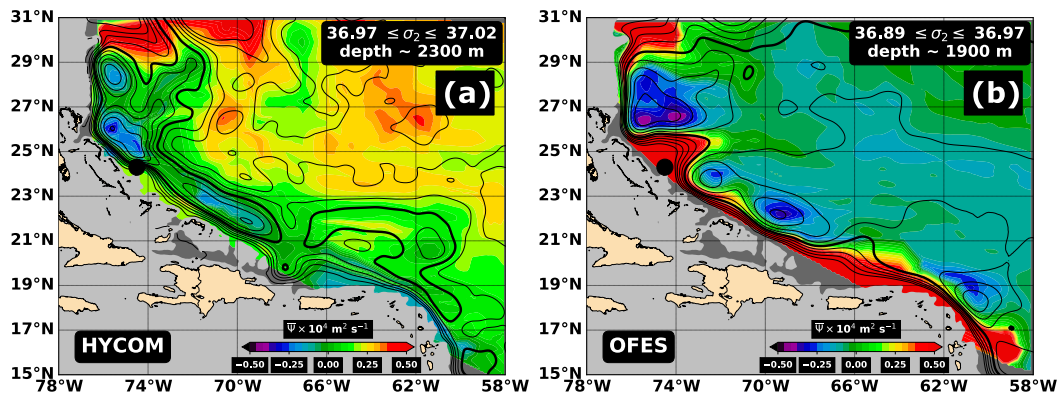FIG. 8. Eddy-forced mean streamfunction distribution $\int_{\overline{q}} -\nabla \cdot \overline{\mathbf{u}'q'}/|\nabla \overline{q}|$ calculated from (a) HYCOM ($36.97 \leq \sigma_2 \leq 37.02$ kg m^{-3}) and (b) OFES ($36.89 \leq \sigma_2 \leq 36.97$ kg m^{-3}) outputs. The continuous black lines represent the total mean streamfunction equally spaced in 10^3 m^2 s^{-1}. The black dot indicates the location of the San Salvador Spur. The boundary condition for the eddy-forced streamfunction was applied along 58°W and consists of the total model streamfunction values at this longitude.
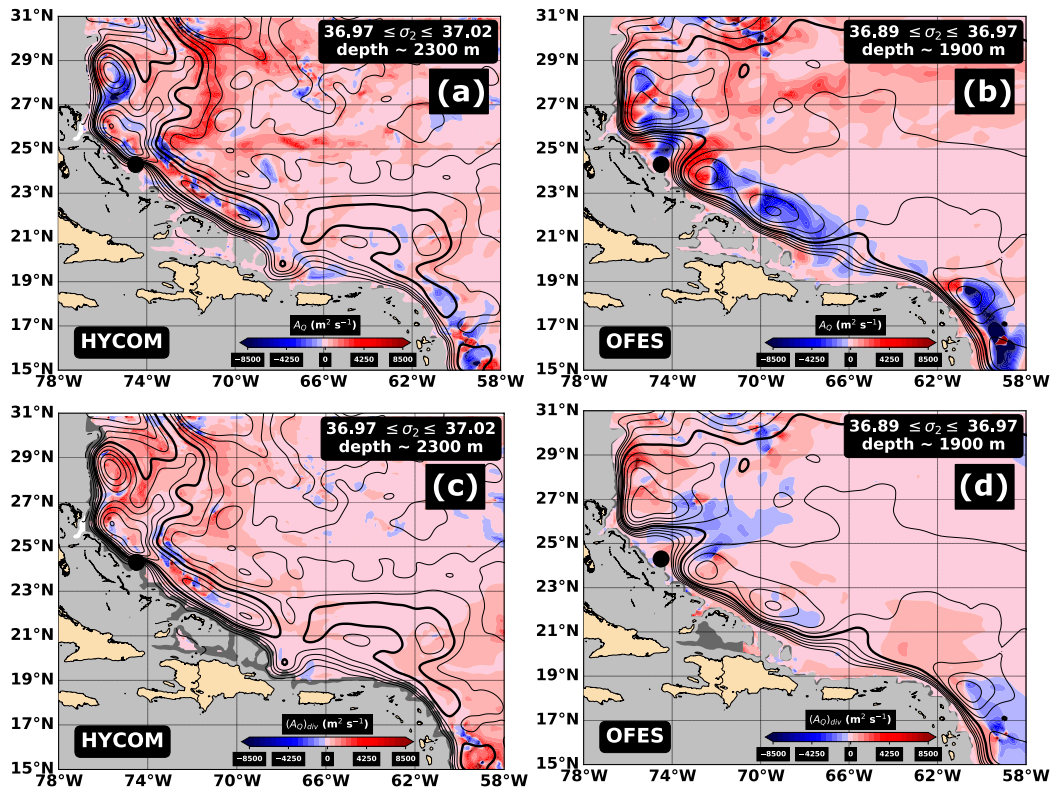
FIG. 9. (a),(b) Austausch coefficients calculated from the total eddy PV fluxes Aq and (c),(d) the nonrotational (or divergent) component of the eddy PV fluxes $(Aq)_{div}$. The continuous black lines represent the total mean streamfunction equally spaced in $10^3 \, \text{m}^2 \, \text{s}^{-1}$. The black dot indicates the location of the San Salvador Spur.

consistent with Leaman and Vertes's (1996) Lagrangian floats trajectories.

The current meter records and OFES outputs analyzed by Biló and Johns (2020) reveal that the DWBC's eddy variability at 26.5°N is strongest near its velocity core and seems to be intrinsic to the deep ocean (e.g., see their Fig. 8). Moreover, the authors show that the DWBC is likely to be baroclinically

unstable, which could lead to the production of meanders and eddies that propagate southward along its path. Instability processes are known to generate downgradient fluxes that act to erode potential vorticity gradients (e.g., Pedlosky 1987; Vallis 2017). From idealized numerical simulations, Spall (1994) showed that instabilities of abyssal boundary currents could force local and basinwide mean recirculations. The
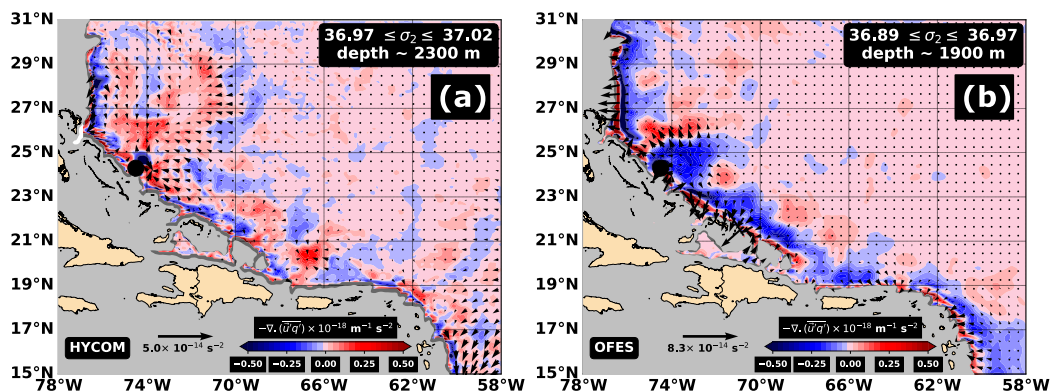

FIG. 10. Nonrotational (or divergent) horizontal eddy potential vorticity flux vectors in (a) HYCOM ($36.97 \leq \sigma_2 \leq 37.02 \, \text{kg m}^{-3}$) and (b) OFES ($36.89 \leq \sigma_2 \leq 36.97 \, \text{kg m}^{-3}$). The black dot indicates the location of the San Salvador Spur.
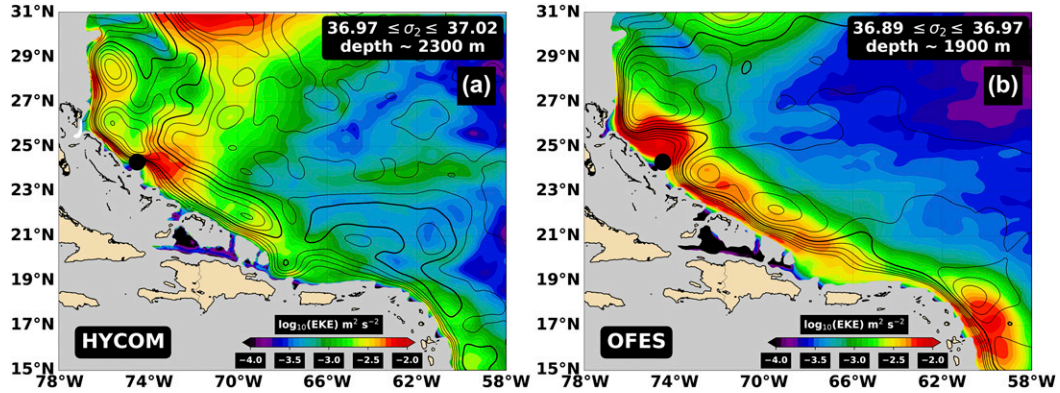
FIG. 11. Eddy kinetic energy (EKE = $\overline{u'^2 + v'^2}/2$) from (a) HYCOM ($36.97 \leq \sigma_2 \leq 37.02$ kg m^{-3}) and (b) OFES ($36.89 \leq \sigma_2 \leq 36.97$ kg m^{-3}) overlaid with mean streamfunction (solid black lines) and potential vorticity (dashed green lines). The streamfunction (potential vorticity) contours are equally spaced in 10^3 m^2 s^{-1} (0.25×10^{-12} m^{-1} s^{-1}). The black dot indicates the location of the San Salvador Spur.

(Aq)$_{\text{div}}$ coefficient presented in Figs. 9c and 9d indicates that the eddy fluxes are consistently downgradient along the DWBC path, reinforcing the hypothesis that the eddy fluxes within the DWBC likely result from active instability processes.

To shed some light on what type of phenomena are involved in producing the convergence of the eddy PV fluxes, it is useful to investigate what time scales account for the covariance between the eddy potential vorticity and velocity perturbations. It is worth mentioning that mean eddy PV fluxes—or the PV covariance—can be dominated by the rotational fluxes components (e.g., Figs. 5b and 10b; Marshall and Shutts 1981; Wilson and Williams 2004), therefore an analysis of the PV/velocity cospectra or coherence (e.g., Emery and Thomson 2001) might highlight time scales that do not affect the PV budget. To focus our analysis on the time scales that contribute to convergence of the mean PV fluxes, we study the $-\nabla \cdot (\mathbf{u}'q')$ evolution in certain critical regions. Figure 12 presents six key locations from each model where the $-\nabla \cdot (\mathbf{u}'q')$ time series

were analyzed. We chose two points within each cyclonic circulation cell north of 19°N that correspond to areas where the mean flow is significantly crossing PV gradients (i.e., large $\overline{\mathbf{u}} \cdot \nabla \overline{q}$). As mentioned in the previous sections, the mean flow is losing PV along the DWBC, while PV is injected into the waters leaving the western boundary. Therefore, the selected points were grouped in locations near the western boundary (points 1, 2, and 3 in Fig. 12) and along the northward recirculation pathways (points 4, 5, and 6).

In Figs. 13a and 13b we plot the cumulative time integral of $-\nabla \cdot (\mathbf{u}'q')$ normalized by the number of time steps. The last data point, therefore, represents the time-mean eddy PV flux convergences $-\nabla \cdot (\overline{\mathbf{u}'q'})$ at each location. This data representation allows the evolution of the eddy PV flux convergence and its steadiness to be evaluated, and highlights important events that cause the convergence to change. In HYCOM, the points along the DWBC (Fig. 13a) are characterized by a persistent (i.e., almost constant) negative accumulation of $-\nabla \cdot (\overline{\mathbf{u}'q'})$ that are interrupted by sudden changes in $-\nabla \cdot (\overline{\mathbf{u}'q'})$
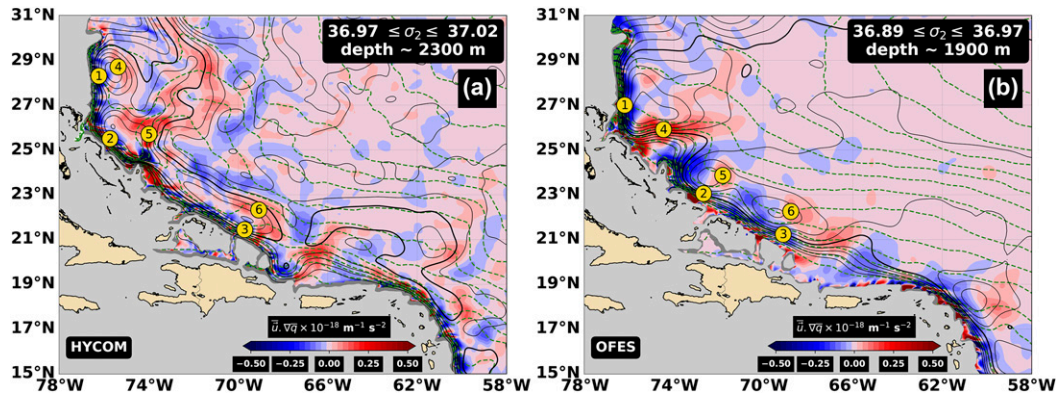

FIG. 12. Mean potential vorticity advection $\overline{\mathbf{u}} \cdot \nabla \overline{q}$ from (a) HYCOM ($36.97 \leq \sigma_2 \leq 37.02$ kg m^{-3}) and (b) OFES ($36.89 \leq \sigma_2 \leq 36.97$ kg m^{-3}) overlaid with mean streamfunction (solid black lines) and potential vorticity (dashed green lines). The streamfunction (potential vorticity) contours are equally spaced in 10^3 m^2 s^{-1} (0.25×10^{-12} m^{-1} s^{-1}). The yellow dots indicate the locations where the $-\nabla \cdot (\mathbf{u}'q')$ time series were analyzed.
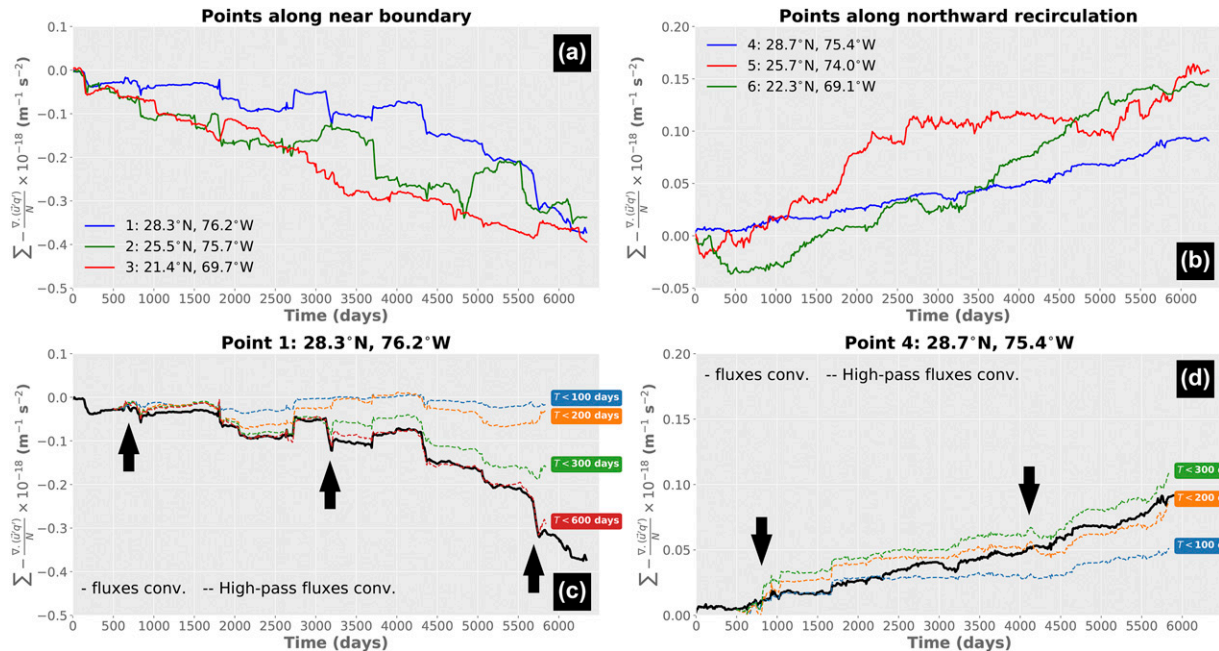
FIG. 13. HYCOM (2000–16) cumulative sum over time of the convergence of eddy potential vorticity fluxes $-\nabla \cdot (\mathbf{u}'q')$ normalized by the number of time steps N at the locations (a) along the western boundary and (b) northward recirculation. (c),(d) Shown are points 1 and 4 original curves (solid lines) and the ones reconstructed from high-passed velocity and potential vorticity series using different cutoffs (dashed lines). Filtering edge effects are avoided by discarding the first and last 500 days of the filtered time series. The black arrows pinpoint specific eddy events.

(e.g., staircase-like features in Fig. 13a). These changes last relatively short periods of time, 250 days or less. In contrast, locations along the northward recirculation (Fig. 13b) present positive convergence accumulation with smaller-amplitude abrupt changes. Although locations 4 (blue curve) and 6 (green curve, from day 500 forward) show a quasi-constant convergence accumulation, point 5 (red curve) is characterized by a noticeable change in the slope of the cumulative curve over long periods of time (i.e., 0–1500, 1500–2500, 2500–5000, and 5000 days forward).

To understand what time scales are involved in this accumulation of $-\nabla \cdot (\overline{\mathbf{u}'q'})$ throughout the time series, we high-passed filtered the $\mathbf{u}'$ and q' time series at each location using a fifth-order Butterworth digital filter with different cutoffs periods (e.g., Emery and Thomson 2001), and reconstructed the cumulative convergence curves. Figures 13c and 13d show the filtered curves for locations 1 and 4 (i.e., northern cell within the Abaco gyre). Note that at both locations, mesoscale time scales between 100 and 300 days reproduce the cumulative curve—i.e., $T < 200$ and $T < 300$ days dashed lines are almost parallel to the thick black line representing all time scales—except for certain events highlighted by the arrows. During these events, longer time scales seem to be required for reproducing their convergence accumulation (e.g., Fig. 13c, $T < 600$ days curve). On the other hand, the accumulation at location 5 (red line in Fig. 13b) is explained by time scales longer than 600 days throughout the time series (not shown).

We repeated the same analysis for locations 1–6 in OFES (Fig. 14). To make the time scales analysis comparable to

HYCOM's, we used the last 17 years from the simulation (i.e., 1997–2013). Similar to HYCOM, all series presented in Figs. 14a and 14b show a steady convergence accumulation interrupted by energetic events, except at location 4. Time scales between 200 and 300 days correspond to the frequency band that contains most of the DWBC transport variability at 26.5°N. Biló and Johns (2020) show that these time scales are related to southward propagating meanders/eddies that seem to be triggered by instability of the DWBC.

Note that HYCOM's location 5 and OFES's location 4 are just to the north of the San Salvador Spur (see Fig. 12), and both show a more "irregular" accumulation that is shown to involve longer time scales in OFES (similar conclusion applies to HYCOM location 5, but not shown). Biló and Johns (2020) showed that, in OFES, the low-frequency variability in the region is dominated by large anticyclonic eddies that slowly propagate northwestward along the western boundary and perturb the Abaco Gyre for several months. Although the low-frequency variability in HYCOM has not been investigated in detail, low-frequency events are found to be similarly important in controlling the eddy PV flux convergences in HYCOM's location 5. Leaman and Vertes (1996) found that the DWBC's position near the San Salvador Spur is crucial for trapping particles within the Abaco Gyre. The authors showed that RAFOS floats released within DWBC remain in (are exported from) the western boundary if the DWBC jet is near (displaced northward of) the San Salvador island. This movement is referred to as the "San Salvador gate" by the authors and might be controlling eddy fluxes convergence in the region.
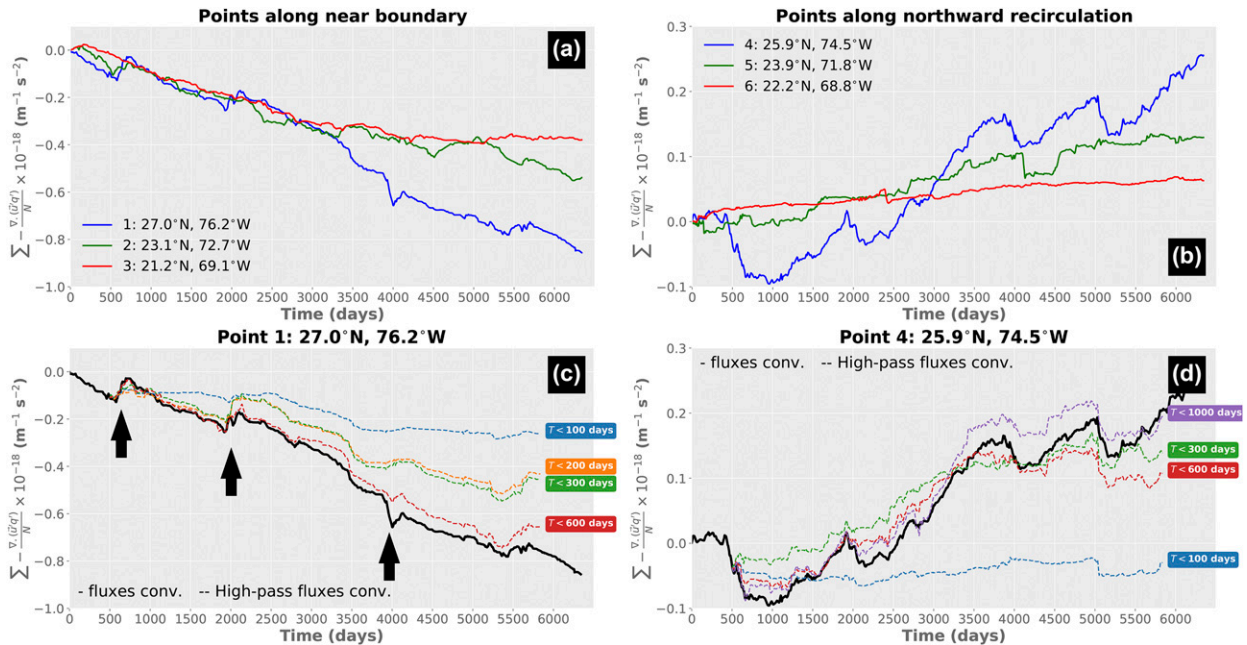
FIG. 14. OFES (1997–2013) cumulative sum over time of the convergence of eddy potential vorticity fluxes $-\nabla \cdot (\mathbf{u}'q')$ normalized by the number of time steps N at the locations (a) along the western boundary and (b) northward recirculation. (c),(d) Shown are points 1 and 4 original curves (solid lines) and the ones reconstructed from high-passed velocity and potential vorticity series using different cutoffs (dashed lines). Filtering edge effects are avoided by discarding the first and last 500 days of the filtered time series. The black arrows pinpoint specific eddy events.

In OFES, the sudden sharp $-\nabla \cdot (\overline{\mathbf{u}'q'})$ changes coincide with the presence of these energetic anticyclonic eddies, which as shown in Biló and Johns's (2020) analysis, sporadically reach 26.5°N every 5–6 years. Due to their slow propagation and abrupt nature, their spectral representation includes a wide range of time scales (200–1500 days, see their Figs. 6 and 7). Therefore, even though their occurrence time scale is long, they can still result in relatively abrupt changes in the cumulative $-\nabla \cdot (\overline{\mathbf{u}'q'})$ when they arrive at specific locations.

4. Summary and conclusions

Using two numerical eddy-resolving simulations with different architectures, we tested if mesoscale eddies drive the deep localized cyclonic cells along the DWBC path between 15° and 30°N. Despite some differences in the recirculation cells in each model, our assessment of the modeled deep isopycnal circulation patterns, mean PV budget [Eq. (2)], and time scales of the perturbations provide compelling evidence that mesoscale eddies are driving these deep recirculations within the $\sigma_2 = 36.77$–$37.06 \, \mathrm{kg \, m^{-3}}$ isopycnals, or the upper North Atlantic Deep Water layer (1000–3000 m).

Our circulation analysis reveals that both simulations reproduce key characteristics of the observed deep circulation. Below 1000 m depth, the DWBC flows southward along the continental slope, and multiple localized cyclonic recirculation cells recirculate waters northward in the interior. Between 15° and 30°N, there are mainly three recirculation areas where PV

is not conserved along the mean recirculation streamlines (i.e., $\overline{\mathbf{u}} \cdot \nabla \overline{q} \neq 0$): the Abaco Gyre (25°–30°N) and the two additional cells offshore the DWBC between 19° and 24°N (e.g., Fig. 3).

The analysis of the mean PV budget reveals that these PV changes (i.e., $\overline{\mathbf{u}} \cdot \nabla \overline{q}$) are mainly due to eddy thickness fluxes—i.e., $-\nabla \cdot (\overline{\mathbf{u}'q'}) \sim -\nabla \cdot (\text{Thick. Flux.})$—except next to the continental slope. Within approximately 100 km of the western boundary, frictional terms in Eq. (2) are not negligible and became the same order of magnitude as the mean PV advection and eddy PV flux convergence terms (Figs. 4–7). Both the reconstructed eddy-driven mean circulation (Fig. 8) and the Aq distributions (Fig. 9), provide additional evidence that eddies force the cyclonic recirculations, homogenizing the PV within closed circulation cells.

The lack of a major upper-ocean boundary current within the study region, and the fact that the largest EKE and $-\nabla \cdot (\overline{\mathbf{u}'q'})$ values are constrained within a few hundreds of kilometers of the western boundary, suggest that the DWBC is the primary source of eddies in the region. Analyzing the time series of $-\nabla \cdot (\mathbf{u}'q')$ along the DWBC and the northward recirculation areas, we found that the mean flow tends to be under an almost continuous eddy forcing (i.e., linear accumulation of $-\nabla \cdot \mathbf{u}'q'$) until relatively fast and large changes in $-\nabla \cdot (\mathbf{u}'q')$ occur (Figs. 13 and 14). The steady eddy forcing is explained mainly by velocity/PV perturbations with periods between 100 and 300 days, which represents the primary variability of the DWBC transport (e.g., Biló and Johns 2020), while the sudden changes seem involve longer time scales. Near the San Salvador Spur, lower-frequency perturbations

are found to be important in contributing to the time mean eddy PV fluxes throughout entire the time series.

To conclude, we believe this study represents the first step toward a quantitative understanding of the mean DWBC recirculation dynamics between 15° and 30°N. Here, we focused on investigating the general mechanism responsible for the recirculation cells. Although we found that eddies near the western boundary likely force these cells, a number of questions remain unanswered about the nature and energy sources for these eddies. First, while the regular 100–300-day period fluctuations that largely control the eddy PV fluxes along the western boundary are believed to be associated with instability of the DWBC, the exact nature of the instability processes affecting the DWBC remains unresolved. Second, the connection between the energetic northwestward propagating anticyclones and the low-frequency time scales controlling the eddy PV fluxes near the San Salvador Spur is unclear in both models. Additionally, the dynamics of such eddies are still not fully understood, despite Biló and Johns's (2020) speculation on their possible formation mechanisms. Therefore, further research on the DWBC instability processes and eddy dynamics in the region will be necessary to achieve a complete understanding of the energy sources for the eddies that drive these deep recirculations.

REFERENCES

Biló, T. C., and W. E. Johns, 2019: Interior pathways of Labrador Sea water in the North Atlantic from the Argo perspective. *Geophys. Res. Lett.*, **46**, 3340–3348, https://doi.org/10.1029/2018GL081439.

——, and ——, 2020: The deep western boundary current and adjacent interior circulation at 24°–30°N: Mean structure and mesoscale variability. *J. Phys. Oceanogr.*, **50**, 2735–2758, https://doi.org/10.1175/JPO-D-20-0094.1.

Bower, A. S., and H. D. Hunt, 2000: Lagrangian observations of the deep western boundary current in the North Atlantic Ocean. Part II: The Gulf Stream–deep western boundary current crossover. *J. Phys. Oceanogr.*, **30**, 784–804, https://doi.org/10.1175/1520-0485(2000)030<0784:LOOTDW>2.0.CO;2.

Bryden, H. L., W. E. Johns, and P. M. Saunders, 2005: Deep western boundary current east of Abaco: Mean structure and transport. *J. Mar. Res.*, **63**, 35–57, https://doi.org/10.1357/0022240053693806.

Emery, W. J., and R. E. Thomson, 2001: *Data Analysis Methods in Physical Oceanography*. Gulf Professional Publishing, 638 pp.

Gary, S. F., S. M. Lozier, C. W. Böning, and A. Biastoch, 2011: Deciphering the pathways for the deep limb of the meridional overturning circulation. *Deep-Sea Res.*, **58**, 1781–1797, https://doi.org/10.1016/j.dsr2.2010.10.059.

Garzoli, S. L., S. Dong, R. Fine, C. S. Meinen, P. C. Renellys, C. Schmid, E. van Sebille, and Q. Yao, 2015: The fate of the deep western boundary current in the South Atlantic. *Deep-Sea Res.*, **103**, 125–136, https://doi.org/10.1016/j.dsr.2015.05.008.

Hogg, N. G., 1983: A note on the deep circulation of the western North Atlantic: Its nature and causes. *Deep-Sea Res.*, **30**, 945–961, https://doi.org/10.1016/0198-0149(83)90050-X.

——, and W. E. Johns, 1995: Western boundary currents. *Rev. Geophys.*, **33**, 1311–1334, https://doi.org/10.1029/95RG00491.

——, R. S. Pickart, R. M. Hendry, and W. J. Smethie, 1986: The northern recirculation gyre of the Gulf Stream. *Deep-Sea Res.*, **33**, 1139–1165, https://doi.org/10.1016/0198-0149(86)90017-8.

Holland, W. R., and P. B. Rhines, 1980: An example of eddy-induced ocean circulation. *J. Phys. Oceanogr.*, **10**, 1010–1031, https://doi.org/10.1175/1520-0485(1980)010<1010:AEOEIO>2.0.CO;2.

Johns, E., R. A. Fine, and R. L. Molinari, 1997: Deep flow along the western boundary south of the Blake Bahama outer ridge. *J. Phys. Oceanogr.*, **27**, 2187–2208, https://doi.org/10.1175/1520-0485(1997)027<2187:DFATWB>2.0.CO;2.

Johns, W. E., T. J. Shay, J. M. Bane, and R. D. Watts, 1995: Gulf Stream structure, transport, and recirculation near 68°W. *J. Geophys. Res.*, **100**, 817–838, https://doi.org/10.1029/94JC02497.

——, L. M. Beal, M. O. Baringer, J. R. Molina, S. A. Cunningham, T. Kanzow, and D. Rayner, 2008: Variability of shallow and deep western boundary currents off the Bahamas during 2004–05: Results from the 26°N RAPID-MOC array. *J. Phys. Oceanogr.*, **38**, 605–623, https://doi.org/10.1175/2007JPO3791.1.

Large, W. G., J. C. McWilliams, and S. C. Doney, 1994: Oceanic vertical mixing: A review and a model with a nonlocal boundary layer parameterization. *Rev. Geophys.*, **32**, 363–403, https://doi.org/10.1029/94RG01872.

Leaman, K. D., and P. S. Vertes, 1996: Topographic influences on recirculation in the deep western boundary current: Results from RAFOS float trajectories between the Blake–Bahama outer ridge and the San Salvador "gate." *J. Phys. Oceanogr.*, **26**, 941–961, https://doi.org/10.1175/1520-0485(1996)026<0941:TIORIT>2.0.CO;2.

Le Bras, I. A., S. R. Jayne, and J. M. Toole, 2018: The interaction of recirculation gyres and a deep boundary current. *J. Phys. Oceanogr.*, **48**, 573–590, https://doi.org/10.1175/JPO-D-17-0206.1.

Lee, T. N., W. E. Johns, R. Zantopp, and F. Schott, 1990: Western boundary current structure and variability east of Abaco, Bahamas at 26.5°N. *J. Phys. Oceanogr.*, **20**, 446–466, https://doi.org/10.1175/1520-0485(1990)020<0446:WBCSAV>2.0.CO;2.

——, ——, R. J. Zantopp, and E. R. Fillenbaum, 1996: Moored observations of western boundary current variability and thermohaline circulation at 26.5°N in the subtropical North Atlantic. *J. Phys. Oceanogr.*, **26**, 962–983, https://doi.org/10.1175/1520-0485(1996)026<0962:MOOWBC>2.0.CO;2.

Li, Z., Y. Chao, and J. C. McWilliams, 2006: Computation of the streamfunction and velocity potential for limited and irregular domains. *Mon. Wea. Rev.*, **134**, 3384–3394, https://doi.org/10.1175/MWR3249.1.

Lozier, S. M., 1997: Evidence for large-scale eddy-driven gyres in the North Atlantic. *Science*, **277**, 361–364, https://doi.org/10.1126/science.277.5324.361.

——, and S. C. Riser, 1989: Potential vorticity dynamics of boundary currents in a quasi-geostrophic ocean. *J. Phys. Oceanogr.*, **19**, 1373–1396, https://doi.org/10.1175/1520-0485(1989)019<1373:PVDOBC>2.0.CO;2.

Lüschow, V., J. von Storch, and J. Marotzke, 2019: Diagnosing the influence of mesoscale eddy fluxes on the deep western boundary current in the 1/10° STORM/NCEP simulation. *J. Phys. Oceanogr.*, **49**, 751–764, https://doi.org/10.1175/JPO-D-18-0103.1.

Maltrud, M. E., R. D. Smith, A. J. Semtner, and R. C. R. C. Malone, 1998: Global eddy-resolving ocean simulations driven by 1985–1995 atmospheric winds. *J. Geophys. Res.*, **103**, 30 825–30 853, https://doi.org/10.1029/1998JC900013.

Marshall, J., and G. Shutts, 1981: A note on rotational and divergent eddy fluxes. *J. Phys. Oceanogr.*, **11**, 1677–1680, https://doi.org/10.1175/1520-0485(1981)011<1677:ANORAD>2.0.CO;2.

Masumoto, Y., and Coauthors, 2004: A fifty-year eddy-resolving simulation of the world ocean: Preliminary outcomes of OFES (OGCM for the Earth Simulator). *J. Earth Simul.*, **1**, 35–56.

Meinen, C. S., and S. L. Garzoli, 2014: Attribution of deep western boundary current variability at 26.5°N. *Deep-Sea Res.*, **90**, 81–90, https://doi.org/10.1016/j.dsr.2014.04.016.

——, W. E. Johns, S. L. Garzoli, E. van Sebille, D. Rayner, T. Kanzow, and M. O. Baringer, 2013: Variability of the deep western boundary current at 26.5°N during 2004–2009. *Deep-Sea Res.*, **85**, 154–168, https://doi.org/10.1016/j.dsr2.2012.07.036.

——, and Coauthors, 2019: Structure and variability of the Antilles current at 26.5°N. *J. Geophys. Res. Oceans*, **124**, 3700–3723, https://doi.org/10.1029/2018JC014836.

Mertens, C., M. Rhein, M. Walter, C. W. Böning, E. Behrens, D. Kieke, R. Steinfeldt, and U. Stöber, 2014: Circulation and transports in the Newfoundland basin, western subpolar North Atlantic. *J. Geophys. Res. Oceans*, **119**, 7772–7793, https://doi.org/10.1002/2014JC010019.

Pedlosky, J., 1987: *Geophysical Fluid Dynamics*. 2nd ed. Springer, 710 pp.

Pickart, R. S., and W. M. Smethie, 1993: How does the deep western boundary current cross the Gulf Stream? *J. Phys. Oceanogr.*, **23**, 2602–2616, https://doi.org/10.1175/1520-0485(1993)023<2602:HDTDWB>2.0.CO;2.

Qiu, B., S. Chen, P. Hacker, N. G. Hogg, S. R. Jayne, and H. Sasaki, 2008: The Kuroshio extension northern recirculation gyre: Profiling float measurements and forcing mechanism. *J. Phys. Oceanogr.*, **38**, 1764–1779, https://doi.org/10.1175/2008JPO3921.1.

Rhines, P. B., and W. R. Holland, 1979: A theoretical discussion of eddy-driven mean flows. *Dyn. Atmos. Oceans*, **3**, 289–325, https://doi.org/10.1016/0377-0265(79)90015-0.

——, and W. R. Young, 1982: Homogenization of potential vorticity in planetary gyres. *J. Fluid Mech.*, **122**, 347–367, https://doi.org/10.1017/S0022112082002250.

Sasai, Y., A. Ishida, Y. Yamanaka, and H. Sasaki, 2004: Chlorofluorocarbons in a global ocean eddy-resolving OGCM: Pathway and formation of Antarctic bottom water. *Geophys. Res. Lett.*, **31**, L12305, https://doi.org/10.1029/2004GL019895.

Sasaki, H., M. Nonaka, Y. Masumoto, Y. Sasai, H. Uehara, and H. Sakuma, 2008: An eddy-resolving hindcast simulation of the quasiglobal ocean from 1950 to 2003 on the Earth Simulator. *High Resolution Numerical Modelling of the Atmosphere and Ocean*, Springer, 157–185.

Schmitz, W. J., and M. S. McCartney, 1993: On the North Atlantic circulation. *Rev. Geophys.*, **31**, 29–49, https://doi.org/10.1029/92RG02583.

Spall, M. A., 1994: Wave-induced abyssal recirculations. *J. Mar. Res.*, **52**, 1051–1080, https://doi.org/10.1357/0022240943076830.

——, 1996: Dynamics of the Gulf Stream/deep western boundary current crossover. Part I: Entrainment and recirculation. *J. Phys. Oceanogr.*, **26**, 2152–2168, https://doi.org/10.1175/1520-0485(1996)026<2152:DOTGSW>2.0.CO;2.

Talley, L. D., G. L. Pickard, W. J. Emery, and J. H. Swift, 2011: *Descriptive Physical Oceanography: An Introduction*. 6th ed. Academic Press, 560 pp.

Toole, J. M., M. Andres, I. A. Le Bras, T. M. Joyce, and M. S. McCartney, 2017: Moored observations of the deep western boundary current in the NW Atlantic: 2004–2014. *J. Geophys. Res. Oceans*, **122**, 7488–7505, https://doi.org/10.1002/2017JC012984.

Vallis, G. R., 2017: *Atmospheric and Oceanic Fluid Dynamics*. 2nd ed. Cambridge University Press, 964 pp.

van Sebille, E., M. O. Baringer, W. E. Johns, C. S. Meinen, L. M. Beal, M. F. de Jong, and H. M. Aken, 2011: Propagation pathways of classical Labrador Sea water from its source region to 26°N. *J. Geophys. Res.*, **116**, C12027, https://doi.org/10.1029/2011JC007171.

——, W. E. Johns, and L. M. Beal, 2012: Does the vorticity flux from Agulhas rings control the zonal pathway of NADW across the South Atlantic? *J. Geophys. Res.*, **117**, C05037, https://doi.org/10.1029/2011JC007684.

Wilson, C., and R. G. Williams, 2004: Why are eddy fluxes of potential vorticity difficult to parameterize? *J. Phys. Oceanogr.*, **34**, 142–155, https://doi.org/10.1175/1520-0485(2004)034<0142:WAEFOP>2.0.CO;2.

Xu, X., W. J. Schmitz, H. E. Hurlburt, P. J. Hogan, and E. P. Chassignet, 2010: Transport of Nordic Seas overflow water into and within the Irminger Sea: An eddy-resolving simulation and observations. *J. Geophys. Res.*, **115**, C12048, https://doi.org/10.1029/2010JC006351.

——, ——, ——, and ——, 2012: Mean Atlantic meridional overturning circulation across 26.5°N from eddy-resolving simulations compared to observations. *J. Geophys. Res. Oceans*, **117**, C03042, https://doi.org/10.1029/2011JC007586.

——, H. E. Hurlburt, W. J. Schmitz, R. Zantopp, J. Fischer, and P. J. Hogan, 2013: On the currents and transports connected with the Atlantic meridional overturning circulation in the subpolar North Atlantic. *J. Geophys. Res. Oceans*, **118**, 502–516, https://doi.org/10.1002/jgrc.20065.

Zhao, J., A. Bower, J. Yang, X. Lin, and N. Penny Holliday, 2018a: Meridional heat transport variability induced by mesoscale processes in the subpolar North Atlantic. *Nat. Commun.*, **9**, 1124, https://doi.org/10.1038/s41467-018-03134-x.

——, J. Yang, S. Semper, R. S. Pickart, K. Våge, H. Valdimarsson, and S. Jónsson, 2018b: A numerical study of interannual variability in the North Icelandic Irminger Current. *J. Geophys. Res. Oceans*, **123**, 8994–9009, https://doi.org/10.1029/2018JC013800.